



Validation of initial observation from the first spaceborne high-spectral-resolution lidar with a ground-based lidar network

Qiantao Liu¹, Zhongwei Huang^{1,2}, Jiqiao Liu^{3,4}, Weibiao Chen^{3,4}, Qingqing Dong¹, Songhua Wu^{5,6}, Guangyao Dai⁵, Meishi Li¹, Wuren Li², Ze Li², Xiaodong Song², and Yuan Xie³

¹Key Laboratory for Semi-Arid Climate Change of the Ministry of Education, College of Atmospheric Sciences, Lanzhou University, Lanzhou, 730000, China

²Collaborative Innovation Center for Western Ecological Safety, Lanzhou University, Lanzhou, 730000, China

³Shanghai Institute of Optics and Fine Mechanics, Chinese Academy of Sciences, Shanghai, 201800, China

⁴Center of Materials Science and Optoelectronics Engineering, University of Chinese Academy of Sciences, Beijing, 100049, China

⁵College of Marine Technology, Faculty of Information Science and Engineering, Ocean University of China, Qingdao, 266100, China

⁶Laoshan Laboratory, Qingdao, 266237, China

Correspondence: Zhongwei Huang (huangzhongwei@lzu.edu.cn)

Received: 9 November 2023 – Discussion started: 13 November 2023

Revised: 20 January 2024 – Accepted: 27 January 2024 – Published: 7 March 2024

Abstract. On 16 April 2022, China successfully launched the world's first spaceborne high-spectral-resolution lidar (HSRL), which is called the Aerosol and Carbon Detection Lidar (ACDL), on board the Atmospheric Environment Monitoring Satellite known as Daqi-1 (DQ-1). The ACDL is expected to precisely detect the three-dimensional distribution of aerosol and cloud globally with high spatial–temporal resolutions. To assess the performance of the newly launched satellite lidar, the ACDL-retrieved observations were compared with ground-based lidar measurements of atmospheric aerosol and cloud over northwest China from May to July 2022 using the Belt and Road lidar network (BR-lidarnet) initiated by Lanzhou University in China and the Cloud-Aerosol Lidar and Infrared Pathfinder Satellite Observation (CALIPSO) lidar observations. A total of six cases in the daytime and nighttime, including clear days, dust events, and cloudy conditions, were selected for further analysis. Moreover, profiles of the total attenuated backscatter coefficient (TABC) and the volume depolarization ratio (VDR) at 532 nm measured by the ACDL, the CALIPSO lidar, and ground-based lidar are compared in detail. Comparison is made between the 532 nm extinction coefficient and lidar ratio obtained from ACDL HSRL retrieval and the Raman retrieval results obtained from BR-lidarnet. The achieved

results revealed that the ACDL observations were in good agreement with the ground-based lidar measurements during dust events with a relative deviation of about $-10.5 \pm 25.4 \%$ for the TABC and $-6.0 \pm 38.5 \%$ for the VDR. Additionally, the heights of the cloud top and bottom from these two measurements were well matched and comparable. Compared with the observation of CALIPSO, the ACDL also shows high consistency. This study proves that the ACDL provides reliable observations of aerosol and cloud in the presence of various climatic conditions, which helps to further evaluate the impacts of aerosol on climate and the environment, as well as on the ecosystem in the future.

1 Introduction

The Aerosol and Carbon Detection Lidar (ACDL) is the first spaceborne high-spectral-resolution lidar (HSRL), which was successfully launched on 16 April 2022 on board the Atmospheric Environment Monitoring Satellite, also known as Daqi-1 (DQ-1). The ACDL is capable of providing a novel perspective on the spatial distribution of atmospheric aerosols and clouds across the globe. An iodine cell is employed to distinct Mie backscattering and Rayleigh backscat-

tering signals from the atmosphere by the ACDL (Dong et al., 2018) so that aerosol and cloud extinction coefficients are precisely retrieved without assuming a lidar ratio (Comerón et al., 2017; Sugimoto and Huang, 2014). Therefore, the ACDL could remarkably enhance the understanding of the crucial roles of aerosols and clouds in global weather and climate change due to their radiative forcing of the Earth's atmosphere system (IPCC, 2013). Still, aerosol inhomogeneity and complex macro- and microphysical processes make them difficult to observe, and they are therefore the most uncertain part of the model. The exploitation of lidar as an effective tool to explore aerosols and clouds has recently been extensively developed due to its active detection and its advantages in better penetration and temporal continuity (Comerón et al., 2017; Sugimoto and Huang, 2014; Huang et al., 2018; Liu et al., 2022; Huang et al., 2022). Thus, spaceborne lidar detection technology can be implemented to observe continuous spatial–temporal aerosol and cloud distribution around the world, thereby compensating for the deficiency in ground-based lidar detection and playing an increasingly prominent role in all current observation approaches (Huang et al., 2018; Liu et al., 2022; Huang et al., 2015; Sugimoto et al., 2012; Huang et al., 2010). The combination of ground observation and satellite observation can be used to evaluate the direct radiative forcing caused by aerosols (Hansell et al., 2010; Lakshmi et al., 2021) and analyse the outbreaks of desert dust (Marcos et al., 2016). Long-term ground-based and spaceborne lidar measurements could be used to understand the vertical and spatial distributions of aerosols (Gupta et al., 2021).

In order to ensure the accuracy and quality of satellite observation, spaceborne lidar data must be appropriately validated by ground-based lidar (Gimmestad et al., 2017). For instance, observations by the Cloud-Aerosol Lidar with Orthogonal Polarization (CALIOP) on board the Cloud-Aerosol Lidar and Infrared Pathfinder Satellite Observation (CALIPSO) satellite have been globally validated. A comparison of CALIPSO and ground-based lidar subjected to various weather conditions was performed through a direct comparison of satellite- and ground-based lidar observations (Tao et al., 2008). An investigation by the European Aerosol Research Lidar Network (EARLINET) of 40 CALIPSO overpass cases was conducted to validate the initial CALIPSO backscattering attenuation coefficients (Mamouri et al., 2009). Chiang et al. (2011) reported the first intercomparison of vertical profiles of aerosols and clouds derived from CALIPSO and ground-based lidar over Chung-Li, Taiwan. The level-2 extinction coefficient profiles of CALIPSO have also been verified by ground-based lidar observations (Giannakaki et al., 2011). In addition, the accuracy and uncertainty of aerosol products obtained by the Visible Infrared Imaging Radiometer Suite (VIIRS) through the Deep Blue algorithm are also compared and evaluated through ground-based observations (He et al., 2021). The HSRL for detecting the optical properties of clouds and

aerosols of the ACDL satellite has been evaluated through CALIPSO (Liu et al., 2019). Currently, another instrument carried on DQ-1 for detecting carbon dioxide is being evaluated more frequently (Wang et al., 2020, 2022; Cao et al., 2022), but the ability of the ACDL to detect aerosol and cloud characteristics has not yet been evaluated using ground-based lidar systems.

The Belt and Road lidar network (BR-lidarnet) led by Lanzhou University can provide real-time data at multiple wavelengths from ultraviolet to near-infrared (i.e. 355, 532, and 1064 nm). Lidar network data are widely employed to validate and assimilate dust transport models to assess the emission, transport, and deposition of dust (Sugimoto and Huang, 2014). Huang et al. (2020) established a good relationship between the absorption coefficients of aerosols and the depolarization ratios of dust aerosols at wavelengths of 532 nm and 355 nm, and in turn, a simple and reliable method was proposed to better identify aerosol and cloud types (Qi et al., 2021). For the specific optical properties of dust aerosol, vertical distributions were derived from observations of the lidar network (Dong et al., 2022; Huang et al., 2023a, b). Likewise, the vertical distributions of dust aerosols and cloud microphysical properties were obtained in the hinterland of the Taklamakan Desert based on polarization Raman lidar observations at the Tazhong site in the lidar network (Zhang et al., 2022, 2023).

To verify the initial and novel retrievals of the ACDL, the vertical structures of aerosol and cloud near dust sources in northwest China measured by BR-lidarnet are implemented in the current work. The paper is structured as follows. Section 2 is comprised of a brief introduction of the basic principles of the ACDL and ground-based lidar observation networks and the methods exploited in this study that allow for direct comparison of the two observations and comparison error assessment. In Sect. 3, we present a comparison of the ACDL and BR-lidarnet observations in the presence of various weather conditions. Finally, we conclude with a summary and discussion of the results in Sect. 4.

2 Lidar systems and methods

2.1 Spaceborne ACDL

The ACDL, on board the satellite DQ-1, is primarily developed by the Shanghai Institute of Optics and Fine Mechanics, Chinese Academy of Sciences. The unique advantage of the ACDL is to precisely detect the global distribution of aerosols and clouds at 532 nm with high spatial–temporal resolutions. By employing an iodine cell filter, Mie scattering and Rayleigh scattering signals at 532 nm are separated (Dong et al., 2018). Additionally, a polarization measurement at 532 nm is very beneficial to distinguish nonspherical particles (dust and ice crystal) from spherical particles (water droplets and sea salt). Moreover, it is also detectable that Mie

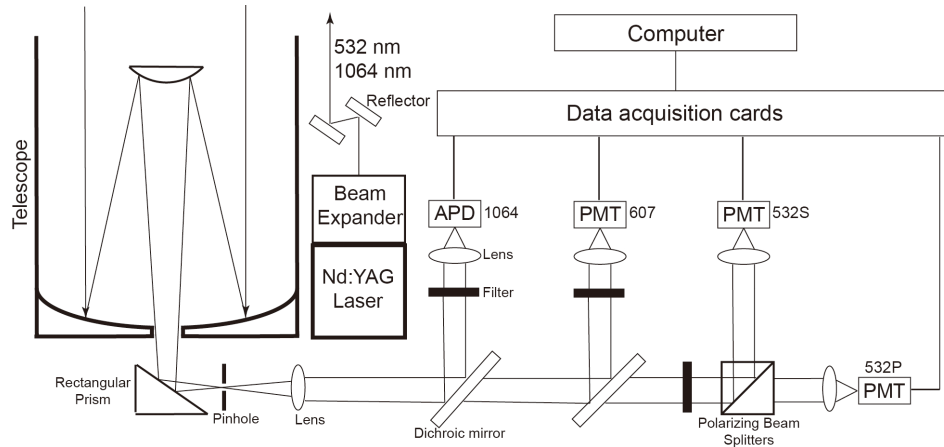


Figure 1. Schematic diagram of the developed ground-based lidar system of BR-lidarnet employed in the present investigation.

scattering signals of aerosol and cloud at the near-infrared wavelength (1064 nm) can be employed to explore the size of particles when combined with measurements at 532 nm. The spatial and temporal resolutions of the ACDL observation are 24 m and 1 min, respectively. The field of view (FOV) of the ACDL is 0.2 mrad, the pulse energy is 150 mJ, and the telescope aperture is Φ 1000 mm (Dong et al., 2018; Liu et al., 2019). The main data products that will be provided by the ACDL in the near future are aerosol and cloud optical parameters, including the aerosol optical depth (AOD), the cloud optical depth (COD), the height of the aerosol and cloud layer, profiles of the backscatter coefficient, the extinction coefficient, and the lidar ratio for aerosol and cloud. For the purpose of validation, the level-2A product of the ACDL is employed, including the total attenuated backscatter coefficient (TABC) and volume depolarization ratio (VDR) at 532 nm using the high-gain channel. By utilizing the HSRL detection channel of the ACDL, we can obtain the extinction coefficient and the lidar ratio at 532 nm.

2.2 Ground-based lidar network (BR-lidarnet)

The ground-based lidar system developed by Lanzhou University is a dual-wavelength polarization Raman lidar used to detect tropospheric aerosol backscatter coefficients at 532 and 1064 nm and the volume depolarization ratio at 532 nm in both the daytime and the nighttime. Additionally, backscattered Raman signal from the atmospheric N_2 molecules at 607 nm can be received at nighttime. The schematic representation of the lidar system exploited in the current investigation has been demonstrated in Fig. 1. The lidar system employs an Nd:YAG laser equipped with a frequency-doubling crystal. The two laser beams at wavelengths of 1064 and 532 nm are collimated and amplified by beam expanders. A Cassegrain telescope is employed to receive backscattering signals from the atmosphere. The backscatter signal with a wavelength of 532 nm is divided

into parallel and perpendicular components by the polarizing beam splitters (PBSs) and is thus detected by the photomultiplier tubes (PMTs), while the 1064 nm signal is detected by an enhanced Si avalanche photodiode (APD). The temporal and spatial resolutions of the observed data are 5 min and 3.75 m, respectively. The FOV of ground-based lidar is 0.5 mrad, the pulse energy is 100 mJ, and the telescope aperture is Φ 200 mm. Raw signals were pre-processed by background correction, range correction, polarization correction, and overlap correction before further analysis (Wang et al., 2018; Huang et al., 2020).

2.3 CALIPSO spaceborne lidar

CALIPSO is designed to understand how clouds and aerosols influence Earth's climate. On 28 April 2006, CALIPSO was launched as a new mission for Earth science observation. CALIPSO is equipped with the cloud–aerosol lidar known as CALIOP (Cloud-Aerosol Lidar with Orthogonal Polarization). The CALIOP system employs two-wavelength elastic backscatter lidar (Winker et al., 2009). Backscatter profiles could be obtained at 532 and 1064 nm along with two orthogonal (parallel and perpendicular) polarization components at 532 nm. A description of the CALIOP data products has already been provided elsewhere (Vaughan et al., 2004). The CALIPSO level-1 data product is used in this study. For a comparison with the ACDL and ground-based lidar, an analysis at 532 nm was conducted.

2.4 Retrieval methodologies

2.4.1 Total attenuated backscatter coefficient (TABC)

For ground-based lidar systems, the elastic lidar equation is given by

$$X(z) = P(z)z^2 = C[\beta_1(z) + \beta_2(z)]T_G^2(z), \quad (1)$$

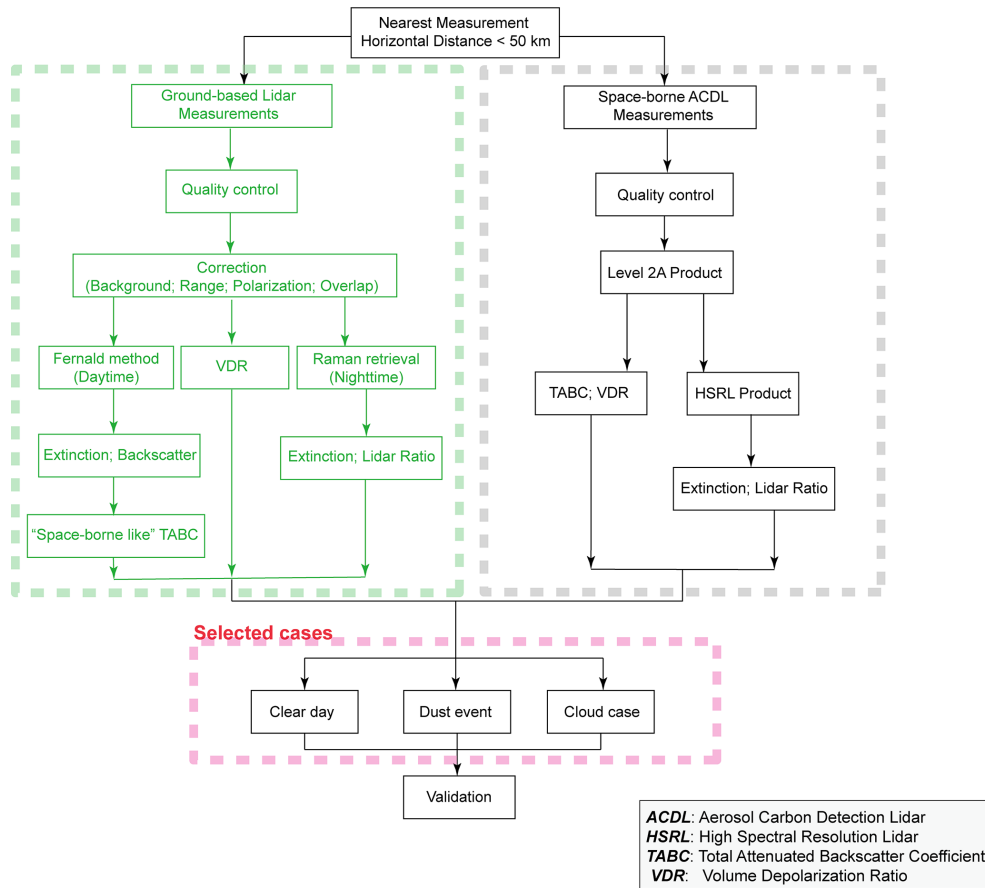


Figure 2. Sketch of the comparison between the ACDL and ground-based lidar in the different weather conditions.

Lidar measurements of aerosol and cloud in the atmosphere over Northwest China on 10 June, 2022

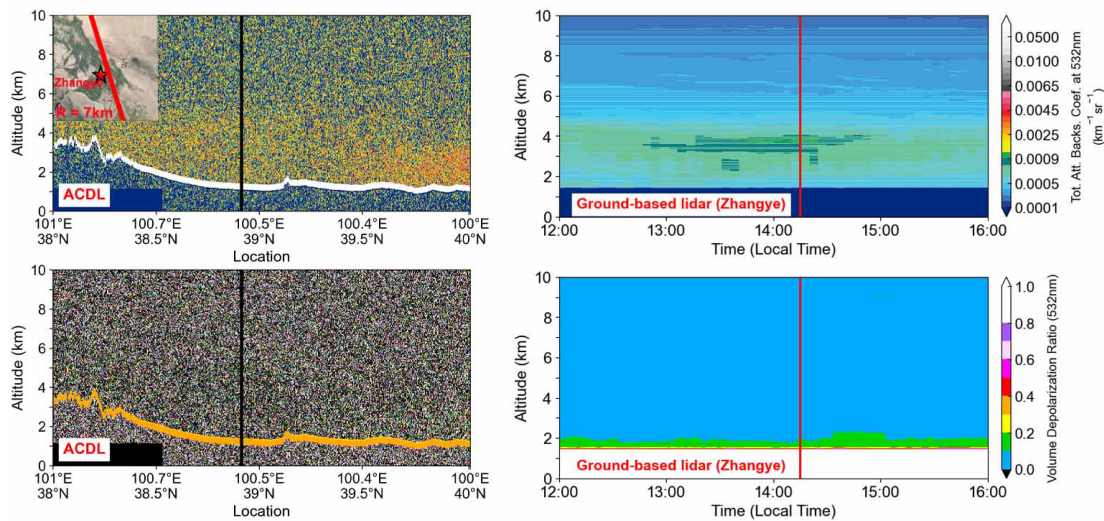


Figure 3. Vertical structure of atmospheric aerosols and clouds observed via the ACDL and the ground-based lidar on 10 June 2022. The solid black line signifies the closest point (7 km) to the Zhangye site in the ACDL overpass track. In the right column, the solid red line corresponds to the ACDL overpass time (14:25 LT). The red pentagram in the upper-left panel indicates the location of the ground-based lidar site and the ACDL track. The map in this figure was exported using © Google Earth (version 10.38.0.0; Apache License, version 2.0, January 2004; <https://www.apache.org/licenses/>, last access: 9 November 2023).

Lidar measurements of aerosol and cloud in the atmosphere over Northwest China on 24 July, 2022

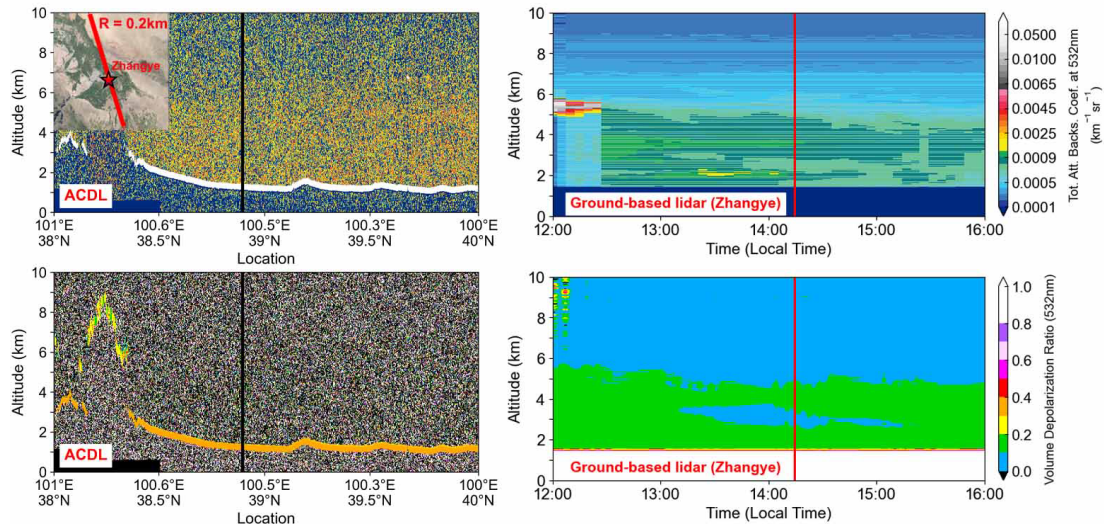


Figure 4. Vertical structure of atmospheric aerosols and clouds observed via the ACDL and the ground-based lidar on the clear day of 24 July 2022. The closest distance between the ACDL track and the ground-based lidar is 0.2 km. The ACDL overpass time is 14:24 LT. The map in this figure was exported using © Google Earth (version 10.38.0.0; Apache License, version 2.0, January 2004; <https://www.apache.org/licenses/>).

Comparison between ACDL and Ground-based lidar observations

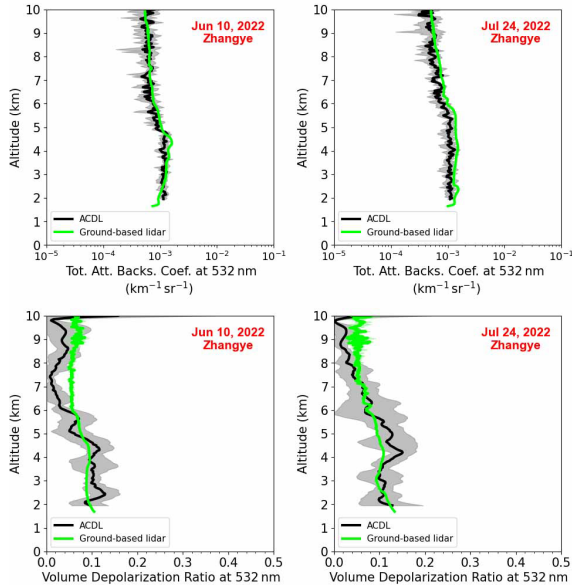


Figure 5. Comparison between the TABC and VDR profiles at 532 nm measured by the ACDL (solid black line) and ground-based lidar (solid lime line) on 10 June and 24 July 2022. The shaded envelope represents the standard deviation.

where $P(z)$ denotes the signal received by the ground-based lidar system from the altitude z ; C represents the lidar system constant; and, finally, $\beta_1(z)$ and $\beta_2(z)$ represent the aerosol and molecule backscatter coefficients at altitude z , respectively. The one-way transmission from the lidar to altitude z

is provided by

$$T_G(z) = \exp \left\{ - \int_0^z [\alpha_1(z') + \alpha_2(z')] dz' \right\}, \quad (2)$$

where $\alpha_1(z)$ and $\alpha_2(z)$ represent the aerosol and molecule extinction coefficients at altitude z , respectively.

For the spaceborne ACDL, the observed backscatter is

$$\beta'_S(z) = [\beta_1(z) + \beta_2(z)] T'_S(z), \quad (3)$$

where

$$T'_S(z) = \exp \left\{ - \int_z^{z_S} [\alpha_1(z') + \alpha_2(z')] dz' \right\},$$

in which z_S denotes the spaceborne lidar calibration altitude.

It is assumed that the directions of both the ground-based and spaceborne lidars that emit laser pulses would be vertical. The above relations indicate that $T'_S(z)/T_G(z)$ increases/decreases with the increase in altitude. Thus, the opposite laser emission directions of the spaceborne and ground-based lidars make the comparison between the two complicated.

In the present study, the attenuated backscatter observed by ground-based lidar is converted to downward attenuated backscatter (Tao et al., 2008), which in turn is utilized to directly compare the spaceborne and ground-based lidar observations. The conversion relation is stated as follows:

$$\beta'_G(z) = [\beta_1(z) + \beta_2(z)] \times \exp \left\{ -2 \int_z^{z_r} [\alpha_1(z') + \alpha_2(z')] dz' \right\}, \quad (4)$$

Lidar measurements of aerosol and cloud in the atmosphere over Northwest China on 29 June, 2022

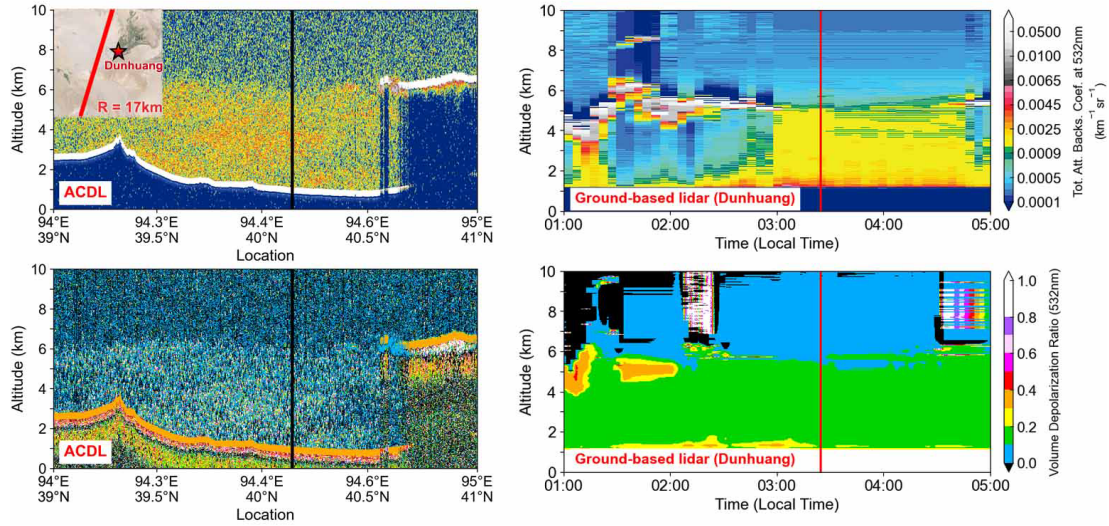


Figure 6. Vertical structure of atmospheric aerosols and clouds observed via the ACDL and the ground-based lidar for a fairly dusty day on 29 June 2022. The closest distance between the ACDL track and the Dunhuang lidar site was 17 km. The ACDL overpass time is 03:41 LT. The map in this figure was exported using © Google Earth (version 10.38.0.0; Apache License, version 2.0, January 2004; <https://www.apache.org/licenses/>).

where z_r denotes the maximum detection height of the ground-based lidar. Few or no aerosols and few molecules are considered to exist between z_r and z_s . Therefore, the function $\beta'_G(z)$ can be employed for comparison with $\beta'_S(z)$. The functions $\beta_2(z)$ and $\alpha_2(z)$ in the above relations are calculated by Mie theory, whereas $\beta_1(z)$ and $\alpha_1(z)$ are retrieved by the conventional Fernald approach (Fernald, 1984). In the retrieval calculation, it is assumed that the lidar ratio is a constant (i.e. does not vary with height) and set to 50 sr. An investigation of uncertainties at $S1 = 50$ sr revealed that the relative errors of the retrieved downward attenuated backscatter at altitudes above 5 km were lower than 5 %, whereas at altitudes below 5 km the errors were as high as 18 % (Tao et al., 2008).

2.4.2 Volume depolarization ratio (VDR) at 532 nm

The volume depolarization ratio is evaluated via the following relation:

$$\delta_{532}(z) = \frac{\beta'_{532s}(z)}{\beta'_{532p}(z)} = \frac{\beta_{532s}(z)T_S^2(z, z_S)}{\beta_{532p}(z)T_S^2(z, z_S)} = \frac{\beta_{532s}(z)}{\beta_{532p}(z)}, \quad (5)$$

where $\beta'_{532s}(z)$ and $\beta'_{532p}(z)$ are the perpendicular and parallel attenuated backscattering coefficients at 532 nm, respectively, whereas $\beta_{532s}(z)$ and $\beta_{532p}(z)$ are the perpendicular and parallel backscattering coefficients at 532 nm, respectively.

The ACDL's volume depolarization ratio could be directly compared with that measured by ground-based lidar because atmospheric transmittance is eliminated in Eq. (5).

2.4.3 Raman method of retrieval by ground-based lidar

The aerosol extinction coefficient using the Raman method (Ansmann et al., 1992) is calculated by

$$\alpha_{\lambda_0}^{aer}(z) = \frac{\frac{d}{dz} \ln \left[\frac{N_R(z)}{P_{\lambda_R}(z)z^2} \right] - \alpha_{\lambda_0}^{mol}(z) - \alpha_{\lambda_R}^{mol}(z)}{1 + \left(\frac{\lambda_0}{\lambda_R} \right)^k}, \quad (6)$$

where $N_R(z)$ is the atmospheric molecular number density of the Raman scattering, and k is the Ångström exponent. The coefficients $\alpha_{\lambda_0}^{mol}(z)$, $\alpha_{\lambda_R}^{mol}(z)$, and $\alpha_{\lambda_0}^{aer}(z)$ are the extinction coefficients. The superscripts aer and mol represent aerosol and molecular, respectively. The subscripts λ_0 (532 nm) and λ_R (607 nm) represent the elastic backscattering wavelength and the Raman scattering wavelength, respectively. $P_{\lambda_R}(z)$ is the Raman backscattering signal.

The aerosol backscatter coefficient measured by Raman lidar is calculated as follows:

$$\beta_{\lambda_0}^{aer}(z) + \beta_{\lambda_0}^{mol}(z) = \left[\beta_{\lambda_0}^{aer}(z_0) + \beta_{\lambda_0}^{mol}(z_0) \right] \times \frac{P_{\lambda_R}(z_0)P_{\lambda_0}(z)N_R(z)}{P_{\lambda_R}(z)P_{\lambda_0}(z_0)N_R(z_0)} \times \frac{\exp \left\{ -\int_{z_0}^z \left[\alpha_{\lambda_R}^{aer}(\xi) + \alpha_{\lambda_R}^{aer}(\xi) \right] d\xi \right\}}{\exp \left\{ -\int_{z_0}^z \left[\alpha_{\lambda_0}^{aer}(\xi) + \alpha_{\lambda_0}^{aer}(\xi) \right] d\xi \right\}}, \quad (7)$$

where the reference height z_0 is chosen at the height where $\beta_{\lambda_0}^{mol}(z_0) \gg \beta_{\lambda_0}^{aer}(z_0)$ so that $\beta_{\lambda_0}^{mol}(z_0) + \beta_{\lambda_0}^{aer}(z_0) \approx \beta_{\lambda_0}^{mol}(z_0)$.

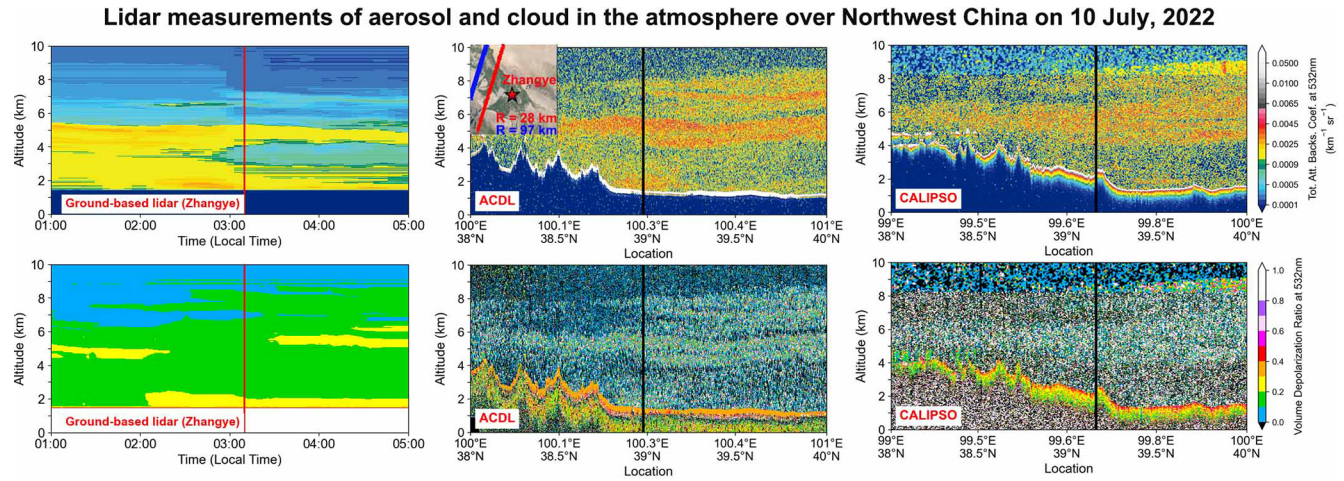


Figure 7. Vertical structure of atmospheric aerosols and clouds observed via the ground-based lidar (left), the ACDL (centre), and CALIPSO (right) on 10 July 2022. The closest distance between the ACDL track (red line) and the Zhangye lidar site is 28 km. The ACDL overpass time is 03:16 LT. The closest distance between the ACDL track and the CALIPSO track (blue line) is 68.65 km. The map in this figure was exported using © Google Earth (version 10.38.0.0; Apache License, version 2.0, January 2004; <https://www.apache.org/licenses/>).

Finally, the lidar ratio profile can be obtained from the profiles of $\alpha_{\lambda_0}^{\text{aer}}(z)$ and $\beta_{\lambda_0}^{\text{aer}}(z)$.

$$S_{\lambda_0}^{\text{aer}}(z) = \frac{\alpha_{\lambda_0}^{\text{aer}}(z)}{\beta_{\lambda_0}^{\text{aer}}(z)} \quad (8)$$

2.4.4 High-spectral-resolution lidar (HSRL) retrieval method from the ACDL

The lidar equations of HSRL are described as follows (Dong et al., 2018):

$$P_C^\perp(z) = \frac{P_0 \eta_1 A_r L}{z^2} (\beta_{\text{mol}}^\perp + \beta_{\text{aer}}^\perp) \times \exp\left(-2 \int_0^z (\alpha_{\text{mol}} + \alpha_{\text{aer}}) d\xi\right), \quad (9)$$

$$P_C^\parallel(z) = \frac{P_0 \eta_2 A_r L}{z^2} (\beta_{\text{mol}}^\parallel + \beta_{\text{aer}}^\parallel) \times \exp\left(-2 \int_0^z (\alpha_{\text{mol}} + \alpha_{\text{aer}}) d\xi\right), \quad (10)$$

$$P_M^\parallel(z) = \frac{P_0 \eta_3 A_r L}{z^2} (T_{\text{mol}} \beta_{\text{mol}}^\parallel + T_{\text{aer}} \beta_{\text{aer}}^\parallel) \times \exp\left(-2 \int_0^z (\alpha_{\text{mol}} + \alpha_{\text{aer}}) d\xi\right), \quad (11)$$

where $P_C^\perp(z)$, $P_C^\parallel(z)$, and $P_M^\parallel(z)$ are the backscattering signal of the perpendicular polarization channel, the parallel polarization channel, and the HSRL channel, respectively. Coefficients β_{mol} and β_{aer} are the backscattering coefficients of

molecular and aerosol, whereas α_{mol} and α_{aer} are the extinction coefficients of molecular and aerosol. Value P_0 is the laser emitting power. Value A_r is the telescope receiving area. $\eta_{1,2,3}$ is the optical efficiency of the receiving optics in each channel, and L is half of the pulse spatial transfer length. Values T_{mol} and T_{aer} are the molecular and aerosol transmittances of the HSRL iodine filter, respectively, and z is the detection distance.

By combining these three equations, the extinction coefficient and backscattering coefficient of atmospheric aerosols can be obtained:

$$\beta_{\text{aer}}(z) = \frac{P_M(z) + P_C(z) \cdot T_{\text{mol}}}{P_M(z) - P_C(z) \cdot T_{\text{aer}}} \beta_{\text{mol}}(z), \quad (12)$$

$$\alpha_{\text{aer}}(z) = -\frac{1}{2} \frac{\partial}{\partial z} \left\{ \ln \left[\frac{P_M(z)}{\beta_{\text{mol}}(z) T_{\text{mol}}} \right] \right\} - \alpha_{\text{mol}}(z). \quad (13)$$

For specific data processing methods such as signal-to-noise ratio processing, the calibration method, and data quality control, please refer to relevant published articles (Liu et al., 2019; Ke et al., 2022; Dai et al., 2023; Zha et al., 2023).

2.4.5 Relative difference between ACDL and ground-based lidar measurements

We use the following relative error relation to assess the difference between two different instruments for the TABC and VDR used in the comparison:

$$\text{bias}(z) = \frac{\text{ACDL}(z) - \text{GB}(z)}{\text{GB}(z)} \times 100, \quad (14)$$

where $\text{ACDL}(z)$ and $\text{GB}(z)$ are the results of the ACDL and ground-based lidar, respectively.

Comparison between ACDL and Ground-based lidar observations

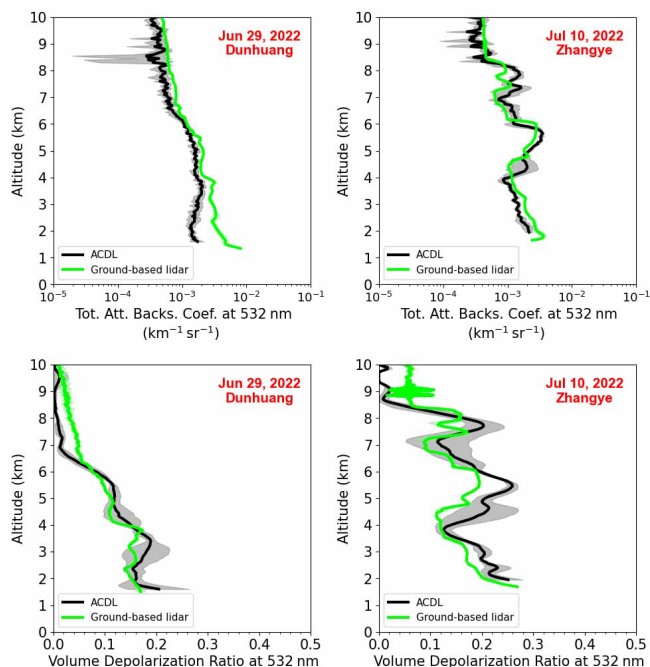


Figure 8. Comparison between the TABC and VDR profiles at 532 nm measured by the ACDL and ground-based lidar on 29 June and 10 July 2022, respectively. The shaded envelope represents the standard deviation.

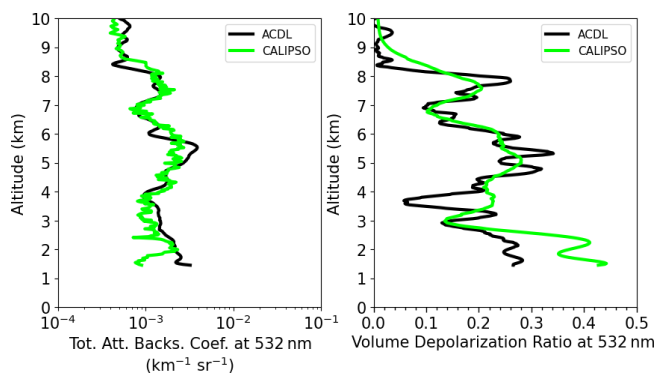


Figure 9. Comparison between the TABC and VDR profiles at 532 nm measured by the ACDL (solid black line) and CALIPSO (solid lime line) on 10 July 2022.

3 Results and discussion

Selecting satellite ground tracks passing within a 50 km radius centred on ground-based lidar for validation. Herein, we compare the six best-matched cases of the spaceborne ACDL that overpassed the ground-based lidar sites in time and space, which are classified into three weather conditions: clear-sky days, dust events, and cloudy conditions. The observation time covers both daytime and nighttime. Among the observations made, the clear-sky cases and one cloudy

case were observed in the daytime, while the other cloudy case and the two dust cases were observed in the nighttime. The other cloudy case and two dust cases in the nighttime were selected. The ground-based lidar sites used for comparison in this study are mainly the Zhangye site (38.9°N , 100.5°E ; 1454 m) and the Dunhuang site (40.1°N , 94.6°E ; 1142 m) in BR-lidarnet. The specific comparison and processing process of data is shown in Fig. 2.

In order to further quantify and visually compare the observed discrepancies between the ACDL and ground-based lidar and to eliminate the uncertainties such as random noise generated by the observations, 21 profiles were averaged in the ACDL (i.e. the profile at the closest distance to the ground site is taken as the centre, and 10 profiles are averaged before and after) and 5 profiles were averaged in the ground-based lidar (i.e. the overpass time was centred and averaged by taking a 10 min profile before and after each of them).

3.1 Clear-day cases

The ACDL overpassed the Zhangye site in BR-lidarnet on 10 June and 24 July 2022. From Figs. 3 and 4, we can observe the presence of low TABC values below 5 km altitude in both cases, and the VDR value is near 0.1. This indicates that there are nearly spherical particles. Meanwhile, the air quality index (AQI) values of these two days are 43 and 45, respectively (where the range of 0–50 is considered to be no pollution), which excludes the possibility of pollution, and therefore these are considered to be clear-sky days.

In terms of the TABC in Fig. 5, both the ACDL and ground-based lidar observed the same vertical distribution characteristics, such as the weaker aerosol layer below 5 km on 10 June. In the altitude range of 2–5 km on 10 June, the maximum values of the TABC measured by the ACDL and ground-based lidar were 0.0014 and $0.0016 \text{ km}^{-1} \text{sr}^{-1}$, respectively. The observation results of the two are basically consistent. On 24 July, the maximum values in the altitude range of 2–6 km were 0.0013 and $0.0015 \text{ km}^{-1} \text{sr}^{-1}$, respectively. The observation results of the two are almost equal. This indicates that for TABC observation under clear weather conditions, the results obtained from the ACDL and ground-based lidar observations are consistent, and the accuracy of the ACDL observation is verified.

The signal-to-noise ratio of the ACDL is lower because the observation time was set to daytime, and the observation results are disturbed by the ambient signal noise, such as sunlight. The VDR values (Fig. 5) of 4–5 km observed by the two on June 10 are consistent, with the ACDL and ground-based lidar observing values of 0.097 and 0.088, respectively. This indicates the presence of spherical particles in this layer. In the case of 24 July, the average VDR of the ACDL and ground-based lidar below 5 km was 0.08 and 0.07, respectively.

Lidar measurements of aerosol and cloud in the atmosphere over Northwest China on 27 May, 2022

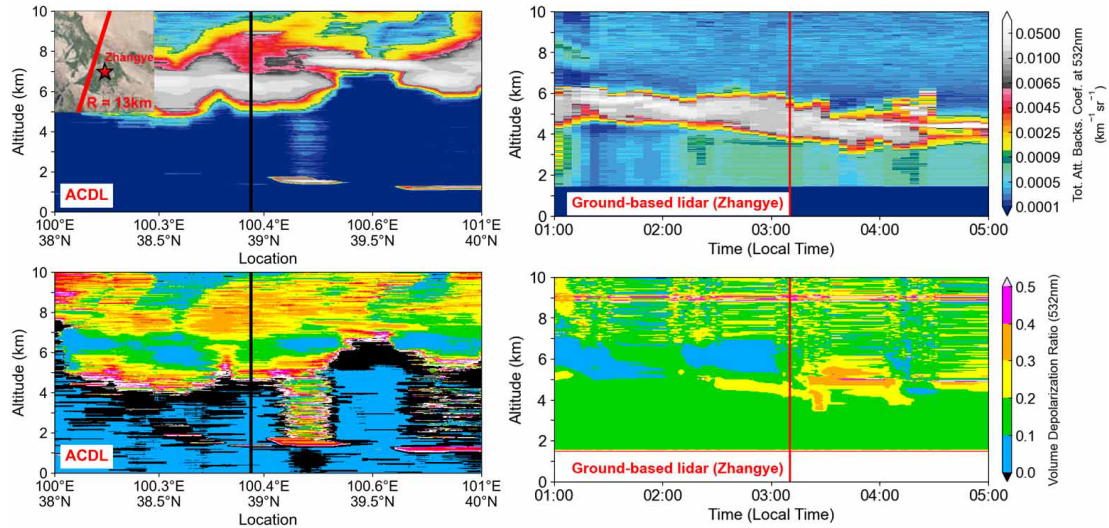


Figure 10. Vertical structure of atmospheric aerosols and cloud observed via the ACDL and the ground-based lidar for a cloudy day on 27 May 2022. The closest distance between the ACDL track and Zhangye lidar site is 13 km, and the overpass time of the ACDL is 03:17 LT. The map in this figure was exported using © Google Earth (version 10.38.0.0; Apache License, version 2.0, January 2004; <https://www.apache.org/licenses/>).

Lidar measurements of aerosol and cloud in the atmosphere over Northwest China on 6 July, 2023

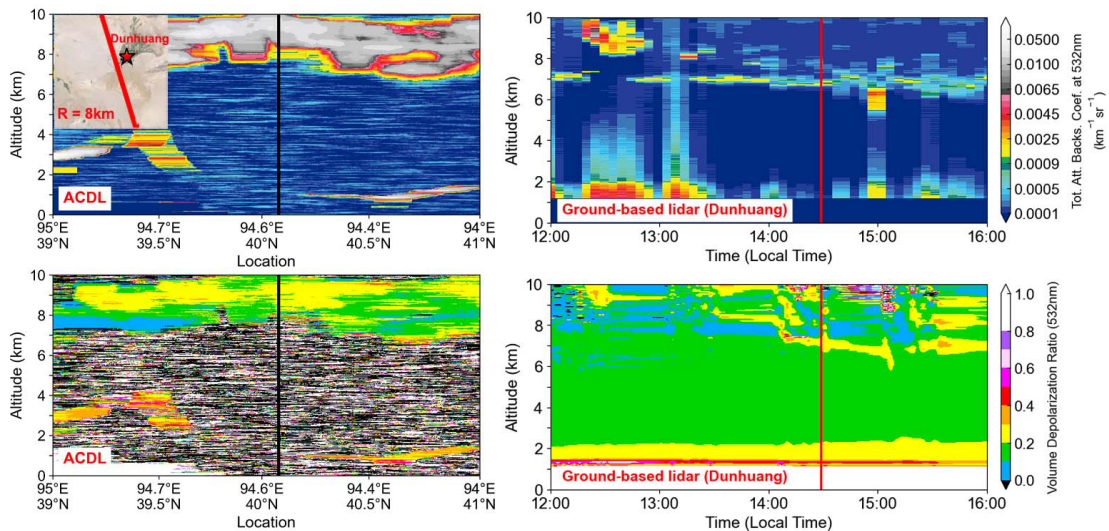


Figure 11. Vertical structure of atmospheric aerosols and clouds observed via the ACDL and the ground-based lidar on 6 July 2022. The closest distance between the ACDL track and the Dunhuang lidar site is 8 km. The ACDL overpass time is 14:48 LT. The map in this figure was exported using © Google Earth (version 10.38.0.0; Apache License, version 2.0, January 2004; <https://www.apache.org/licenses/>).

3.2 Dust cases

The ACDL overpassed the Dunhuang and Zhangye sites in BR-lidarnet on 29 June and 10 July 2022, respectively. Figure 6 illustrates that both the ACDL and ground-based lidar could detect the presence of a thick aerosol layer below 6 km with TABC values of 0.0017 and 0.0031 $\text{km}^{-1} \text{sr}^{-1}$, respectively. The VDR values reached 0.14 and 0.13, respec-

tively, which indicate the existence of nonspherical particles and therefore are considered to be a dust layer. According to the ground-based lidar observation, the dust layer lasted for about 2 h.

The results in Fig. 7 revealed that on 10 July over the Zhangye site, both the ACDL and ground-based lidar could detect the presence of a three-layer aerosol structure, but the third layer of aerosol observed by ground-based lidar is

Comparison between ACDL and Ground-based lidar observations

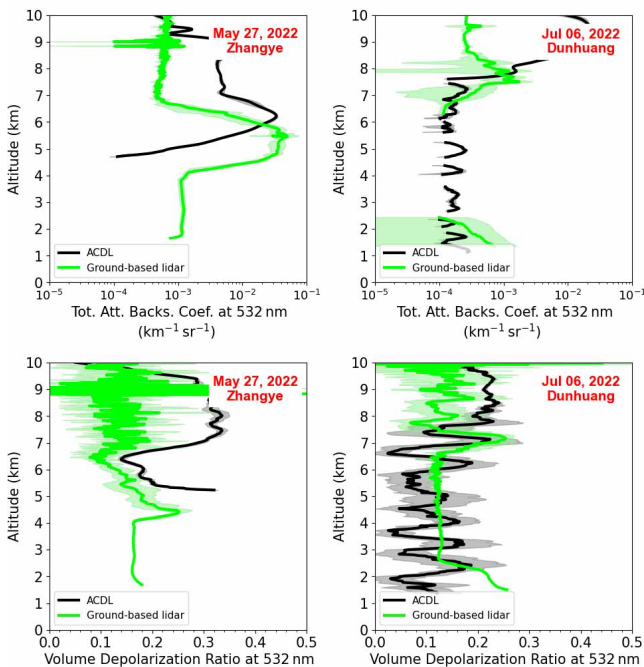


Figure 12. Comparison between the TABC and VDR profiles at 532 nm measured by the ACDL (solid black line) and ground-based lidar (solid lime line) on 27 May and 6 July 2022, respectively. The shaded envelope represents the standard deviation.

relatively thin, corresponding to altitudes of 2–3, 4–6, and 7–8 km above sea level, respectively. The observed and retrieved TABC values based on the ACDL and ground-based lidar in order were 0.0017 and $0.0023 \text{ km}^{-1} \text{ sr}^{-1}$ in the altitude interval of 2–3 km, 0.0021 and $0.002 \text{ km}^{-1} \text{ sr}^{-1}$ in the range of 4–6 km, and 0.0019 and $0.0017 \text{ km}^{-1} \text{ sr}^{-1}$ in the range of 7–8 km. Similarly, the VDR values for the ACDL and ground-based lidar observations are 0.21 and 0.18 (for the altitude range of 2–3 km), and 0.21 and 0.17 (for the altitude of 4–6 km), 0.2 and 0.16 (for the range of 7–8 km). The observed VDR values represent the nonspherical particles and therefore could be judged as dust layers. The dust stratification is more noticeable as seen from the VDR values of the ground-based lidar.

Meanwhile, on 10 July, there was a transit of the CALIPSO satellite. The shortest distance between CALIPSO and ACDL observation trajectories is 68.65 km with a time difference of 80 min between passing through the Zhangye site. The CALIPSO observation is consistent with the one from the ACDL, and three layers of dust layers are observed (see the right column of Fig. 7).

By further quantifying and comparing the discrepancies between the results of the ACDL and those of the ground-based lidar, the observations of the ACDL and those of the ground-based lidar are in better agreement in the presence of dust aerosol (see Fig. 8). In Dunhuang, a dust layer below

6 km was observed by both the ACDL and ground-based lidar (see the left column of Fig. 8). The comparison shows that the TABC values below 4 km based on the ground-based lidar are larger ($0.0036 \text{ km}^{-1} \text{ sr}^{-1}$) than those based on the ACDL ($0.0021 \text{ km}^{-1} \text{ sr}^{-1}$), probably due to the inability of the ACDL laser to penetrate the thick dust layer when observed from above, but above 4 km the ACDL values correspond better. The comparison of observations at the Zhangye site is more consistent, and the three dust layers correspond well to one another in height (see Fig. 8 right). The bias of the TABC on dusty days is $-10.5 \pm 25.4 \%$.

According to the VDR observation values, the aerosol layer positions are all between 0.2–0.3 as dust aerosols. The same dust layer positions are observed by both the ACDL and ground-based lidar. The comparison of VDR values at the two sites is consistent in both cases, and the bias of VDR on the dusty day was $-6.0 \pm 38.5 \%$. However, the signal-to-noise ratio of the ACDL observation results is slightly lower than that of ground-based lidar.

Comparing the observation results of CALIPSO and the ACDL (see Fig. 9), it is found that the two observations are almost identical and have good consistency. In terms of both the observed values and the structure of the dust layer, the ACDL observation results show good consistency with the CALIPSO observation results.

3.3 Cloudy-day cases

The ACDL overpassed the Zhangye and Dunhuang sites in BR-lidarnet on 27 May and 6 July 2022, respectively. The ACDL observation on the left in Fig. 10 reveals that the clouds spread over a large area with the horizontal extent of the clouds greater than 200 km. The observed cloud base and cloud top heights are 5 and 10 km, respectively. The historical weather record also shows a cloudy condition over Zhangye on that day. According to the VDR, the value is around 0.4, which is considered to be a cirrus cloud. The cloud is identified as stratiform based on the spatial distribution characteristics observed by the ACDL. The low signal-to-noise ratio below 6 km is probably due to the fact that the ACDL laser signal does not penetrate deeply into the cloud, and the signal is scattered and attenuated several times within the cloud. Based on the ground-based lidar observation on the right side of Fig. 10, the cloud is very long-lived and existed during the observation period. The heights of the cloud base and top in order are 4 and 7 km, which are lower than the height observed by the ACDL. The VDR values indicate the presence of ice crystals within the cloud, which is a cirrus cloud. The signal-to-noise ratio is reduced above 5 km as seen from the VDR signal, probably because the cloud layer is too thick, and the laser from the ground-based lidar cannot be effectively penetrated; furthermore, the signal is scattered and attenuated several times inside the cloud, which also leads to the reduced signal-to-noise ratio.

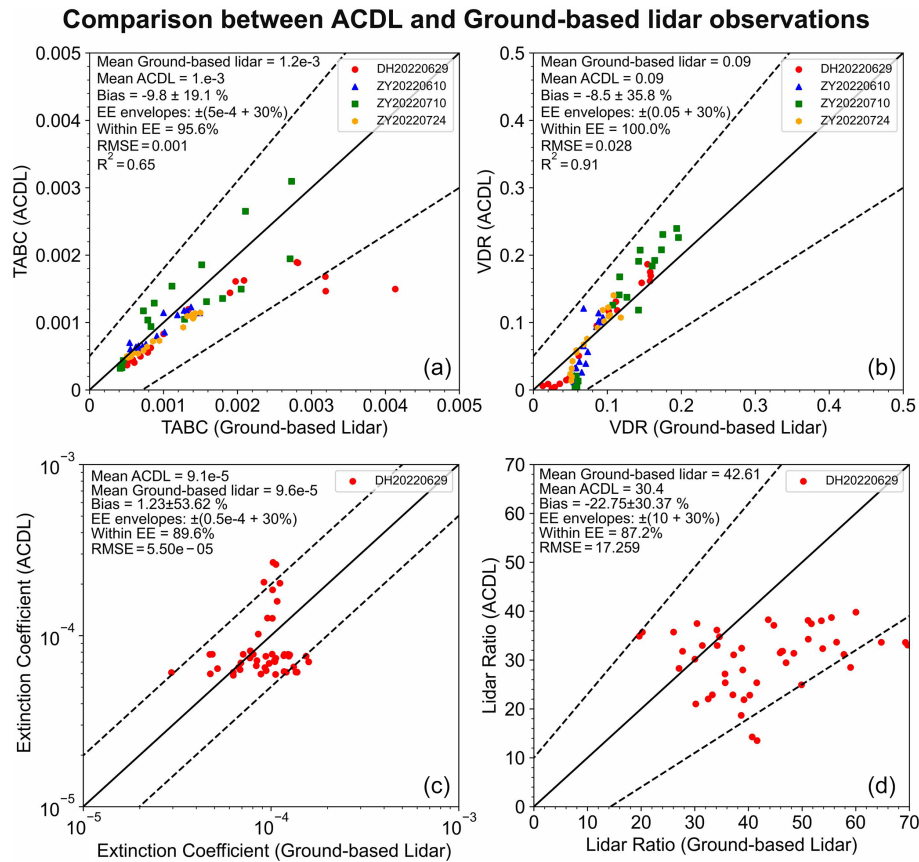


Figure 13. Scatterplots of the ground-based-lidar-retrieved (a) TABC and (b) VDR versus the ACDL measurement under cloud-free conditions. The solid line refers to the 1 : 1 line and the dashed line refers to the expected error envelope, $EE = \pm(0.0005 + 0.3 \times TABC_{Ground})$ and $EE = \pm(0.05 + 0.3 \times VDR_{Ground})$. Panels (c) and (d) show the comparison between the extinction coefficient and lidar ratio obtained from the ACDL and ground-based lidar retrieval under the dust case on 29 June. The solid line refers to the 1 : 1 line and the dashed line refers to the expected error envelope, $EE = \pm(0.5 \times 10^{-4} + 0.3 \times Ext_{Ground})$ and $EE = \pm(10 + 0.3 \times LR_{Ground})$.

Table 1. Summary of ACDL passes over the ground-based lidar sites.

Observed time (yyyy.mm.dd, local time)	Overpassed site	Closest distance point	Closest distance (km)	Weather condition	TABC bias (%)	VDR bias (%)
2022.06.10, 14:25	Zhangye	100.5° E, 38.9° N	7.0	Clear	-3.93 ± 13.62	-16.28 ± 35.79
2022.07.24, 14:24	Zhangye	100.5° E, 38.9° N	0.2	Clear	-14.49 ± 12.04	-5.73 ± 30.49
2022.06.29, 03:41	Dunhuang	94.6° E, 40.1° N	17.3	Dust	-25.15 ± 18.84	-18.24 ± 40.79
2022.07.10, 03:16	Zhangye	100.5° E, 38.9° N	28.6	Dust	4.25 ± 32.01	6.27 ± 36.23
2022.05.27, 03:17	Zhangye	100.5° E, 38.9° N	13.0	Cloudy	-8.33 ± 30.53	-9.07 ± 54.96
2022.07.06, 14:48	Dunhuang	94.6° E, 40.1° N	8.4	Cloudy	-4.68 ± 23.59	-6.12 ± 41.57

On 6 July, the Dunhuang site also recorded a cloudy day as observed from historical weather. Thick clouds in the altitude range of 8–10 km were observed by the ACDL (see Fig. 11), but TABC from ground-based lidar only showed a thin high-value area at 7.5 km. Based on the VDR of ground-based lidar, it was observed that the signal-to-noise ratio is reduced above 7 km, probably due to the presence of thick clouds, which causes the lidar laser not to penetrate the

clouds, thus resulting in a bias between the inversion and the observation. The VDR value observed by both the ACDL and ground-based lidar was 0.3, which probably depicted a mixed-phase cloud composed of ice crystals and supercooled liquid droplets.

Through further quantification to compare the discrepancy in observations between the ACDL and the ground-based lidar, the height of clouds obtained by the ground-based li-

dar is lower than that obtained by the ACDL (see Fig. 12). However, both observations show similar cloud structures. It is also apparent that for the ACDL observations, the signal-to-noise ratio in the presence of the clouds is lower, so the profile is not smooth. Based on the ground-based lidar observations, the signal-to-noise ratio above the cloud is lower. This issue is mainly attributed to the attenuation of the signal by the clouds.

3.4 Comparison of ACDL and ground-based lidar observations

Since the presence of clouds affects the observations and retrievals, we focus on four distinct cases under cloud-free conditions (see Fig. 13). In general, these two observations are in better agreement. In particular, the results of the VDR are better with an observed bias of $-8.5 \pm 35.8\%$ and R^2 of 0.91. The observation results used for comparison are all within the expected error (EE) lines. The overall data sample of the TABC is closer to the 1 : 1 line, with an observed bias of $-9.8 \pm 19.1\%$ and R^2 of 0.65.

Because the Raman channels can only be detected at night, the dust case of the ACDL overpassing the Dunhuang site on 29 June was selected to compare the 532 nm extinction coefficient and lidar ratio obtained by the ground-based lidar Raman retrieval method and the ACDL HSRL retrieval method (bottom row of Fig. 13). The extinction coefficients obtained by the two are relatively consistent, with a bias of $1.23 \pm 53.62\%$. The bias of the lidar ratio is $-22.75 \pm 30.37\%$.

The discrepancies in the comparison between the ACDL and ground-based lidar measurement are possible because of several factors such as different lidar system parameters and the difference in detection distance between spaceborne and ground-based systems and also can be due to the inhomogeneity of the atmosphere (Chiang et al., 2011; Belegante et al., 2018). Overall, the observation comparison results between the ACDL and ground-based lidar are acceptable.

4 Conclusions

In this work, initial observations from the first high-resolution spaceborne lidar were validated against the ground-based lidar network. The ACDL-retrieved profiles of the TABC and VDR of level-2A products are compared with the coincident lidar measurements for the six cases (see Table 1 for a detailed summary). Due to the inhomogeneous horizontal distribution of aerosols in the lower troposphere and clouds, there are some differences between cloud and boundary layer lidar measurements. We first convert the detection direction of the ground-based lidar to the same direction as the ACDL and then compare the observation and retrieval results of these lidars under three weather conditions (i.e. clear-sky, dust, and cloudy).

For clear days, both lidars observed the same vertical distribution characteristics. Since both individual observations for clear days are in the daytime, the overall signal-to-noise ratio is lower due to the influence of the ambient noise. On the other hand, the observed results of the VDR from both lidars are relatively consistent.

In the presence of dust aerosols, the retrieval results of the ACDL and ground-based lidar match better and both could observe the same structure of the dust layer. In the case of a thicker dust layer, it could cause the ACDL to fail to penetrate, so there would be some deviation between the two results near the ground. Since both individual observations are conducted at nighttime, the signal-to-noise ratio is high and the observations are in good agreement. The calculated biases of the TABC and VDR in order are $-10.5 \pm 25.4\%$ and $-6.0 \pm 38.5\%$, respectively. In addition, corresponding to the dust case on 10 July, there is an overpass of the CALIPSO satellite, and it is found that the observation results of the ACDL and CALIPSO are highly consistent.

In the presence of a thicker layer of clouds, the comparison indicated that the cloud height obtained from the ground-based lidar inversion is lower than the one observed by the ACDL due to the presence of thick clouds that block the laser transmission.

In the absence of clouds, both lidars provide better results for the VDR with an observed deviation of $-8.5 \pm 35.8\%$ and R^2 of 0.91. The observed bias of the TABC values is $-9.8 \pm 19.1\%$, and R^2 is 0.65.

Finally, one of the detection advantages of the ACDL is high spectral lidar detection, which can retrieve the extinction coefficient and the lidar ratio profile of aerosols without assuming the lidar ratio. In order to compare the accuracy of its HSRL detection, the extinction coefficient obtained from the Raman channel retrieval of the ground-based lidar was compared with the lidar ratio and the ACDL results. Because the Raman channels can only be detected at night, and combined with the comparison results of the ACDL and ground-based lidar in terms of the TABC and VDR, the dust case on 29 June was selected for validation. The comparison results showed that for the case of the ACDL passing through Dunhuang, the extinction coefficient profiles obtained by the two were relatively close, with a total bias of $1.23 \pm 53.62\%$. The bias of the lidar ratio is $-22.75 \pm 30.37\%$.

The present exploration proves that the ACDL provides a reliable observation of aerosols and clouds subjected to various conditions, which helps to further evaluate the effects of aerosol on climate and environment, as well as on the ecosystem in the future. However, there are still some discrepancies between the two observations, and more ground-based lidar observation should be employed for the validation of the ACDL on a global scale in the future.

Data availability. The ACDL data we used in this paper were not available publicly at the time when the article was submitted. We

are allowed to access the data through our participation as a part of the ACDL scientific team. The CALIPSO lidar observation data are freely available from the Atmospheric Science Data Center (ASDC) website (<https://subset.larc.nasa.gov/calipso/>, last access: 9 November 2023; NASA, 2023).

Author contributions. QL performed the analysis and wrote the paper. JL, GD, and XS provided the original data. QD and ML helped with the methods used in the article. WL and ZL provided technical support. QL and ZH interpreted the results. ZH and JL provided significant input to interpret and improve the paper. All authors discussed the results and commented on the paper.

Competing interests. The contact author has declared that none of the authors has any competing interests.

Disclaimer. Publisher's note: Copernicus Publications remains neutral with regard to jurisdictional claims made in the text, published maps, institutional affiliations, or any other geographical representation in this paper. While Copernicus Publications makes every effort to include appropriate place names, the final responsibility lies with the authors.

Acknowledgements. This work was supported in part by the Second Tibetan Plateau Scientific Expedition and Research programme (STEP; grant no. 2019QZKK0602); the Gansu Provincial Science and Technology Innovative Talent Program: High-level Talent and Innovative Team Special Project (grant no. 22JR9KA001); and the Fundamental Research Funds for the Central Universities (grant nos. lzujbky-2022-kb10 and lzujbky-2022-kb11). The authors would like to thank the operators for providing ACDL level-2 data and HSRL channel data. The data of ground-based lidar in BR-lidarnet were provided by the corresponding author. The maps in the figures were exported using Google Earth (version 10.38.0.0; Apache License, version 2.0, January 2004; <https://www.apache.org/licenses/>, last access: 9 November 2023); we use the data from the website (<https://google.cn/earth/>, last access: 9 November 2023), and we have adhered to their redistribution permissions.

Financial support. This research has been supported in part by the Second Tibetan Plateau Scientific Expedition and Research programme (STEP; grant no. 2019QZKK0602); the Gansu Provincial Science and Technology Innovative Talent Program: High-level Talent and Innovative Team Special Project (grant no. 22JR9KA001); and the Fundamental Research Funds for the Central Universities (grant nos. lzujbky-2022-kb10 and lzujbky-2022-kb11).

Review statement. This paper was edited by Yuanjian Yang and reviewed by three anonymous referees.

References

- Ansmann, A., Wandinger, U., Riebesell, M., Weitkamp, C., and Michaelis, W.: Independent measurement of extinction and backscatter profiles in cirrus clouds by using a combined Raman elastic-backscatter lidar, *Appl. Optics*, 31, 7113, <https://doi.org/10.1364/AO.31.007113>, 1992.
- Belegante, L., Bravo-Aranda, J. A., Freudenthaler, V., Nicolae, D., Nemuc, A., Ene, D., Alados-Arboledas, L., Amodeo, A., Pappalardo, G., D'Amico, G., Amato, F., Engelmann, R., Baars, H., Wandinger, U., Papayannis, A., Kokkalis, P., and Pereira, S. N.: Experimental techniques for the calibration of lidar depolarization channels in EARLINET, *Atmos. Meas. Tech.*, 11, 1119–1141, <https://doi.org/10.5194/amt-11-1119-2018>, 2018.
- Cao, X., Zhang, L., Zhang, X., Yang, S., Deng, Z., Zhang, X., and Jiang, Y.: Study on the Impact of the Doppler Shift for CO₂ Lidar Remote Sensing, *Remote Sens.*, 14, 4620, <https://doi.org/10.3390/rs14184620>, 2022.
- Chiang, C.-W., Kumar Das, S., Shih, Y.-F., Liao, H.-S., and Nee, J.-B.: Comparison of CALIPSO and ground-based lidar profiles over Chung-Li, Taiwan, *J. Quant. Spectrosc. Ra.*, 112, 197–203, <https://doi.org/10.1016/j.jqsrt.2010.05.002>, 2011.
- Comerón, A., Muñoz-Porcar, C., Rocadenbosch, F., Rodríguez-Gómez, A., and Sicard, M.: Current Research in Lidar Technology Used for the Remote Sensing of Atmospheric Aerosols, *Sensors*, 17, 1450, <https://doi.org/10.3390/s17061450>, 2017.
- Dai, G., Wu, S., Long, W., Liu, J., Xie, Y., Sun, K., Meng, F., Song, X., Huang, Z., and Chen, W.: Aerosols and Clouds data processing and optical properties retrieval algorithms for the spaceborne ACDL/DQ-1, EGU sphere [preprint], <https://doi.org/10.5194/egusphere-2023-2182>, 2023.
- Dong, J., Liu, J., Bi, D., Ma, X., Zhu, X., Zhu, X., and Chen, W.: Optimal iodine absorption line applied for spaceborne high spectral resolution lidar, *Appl. Optics*, 57, 5413, <https://doi.org/10.1364/AO.57.005413>, 2018.
- Dong, Q., Huang, Z., Li, W., Li, Z., Song, X., Liu, W., Wang, T., Bi, J., and Shi, J.: Polarization Lidar Measurements of Dust Optical Properties at the Junction of the Taklimakan Desert–Tibetan Plateau, *Remote Sens.*, 14, 558, <https://doi.org/10.3390/rs14030558>, 2022.
- Fernald, F. G.: Analysis of atmospheric lidar observations: some comments, *Appl. Optics*, 23, 652–653, <https://doi.org/10.1364/AO.23.000652>, 1984.
- Giannakaki, E., Vraimaki, E., and Balis, D.: Validation of CALIPSO level-2 products using a ground based lidar in Thessaloniki, Greece, *Proc. SPIE*, 818215, <https://doi.org/10.1117/12.898124>, 2011.
- Gimmetstad, G., Forrister, H., Grigas, T., and O'Dowd, C.: Comparisons of aerosol backscatter using satellite and ground lidars: implications for calibrating and validating spaceborne lidar, *Sci. Rep.*, 7, 42337, <https://doi.org/10.1038/srep42337>, 2017.
- Gupta, G., Ratnam, M. V., Madhavan, B. L., Prasad, P., and Narayanamurthy, C. S.: Vertical and spatial distribution of elevated aerosol layers obtained using long-term ground-based and space-borne lidar observations, *Atmos. Environ.*, 246, 118172, <https://doi.org/10.1016/j.atmosenv.2020.118172>, 2021.
- Hansell, R. A., Tsay, S. C., Ji, Q., Hsu, N. C., Jeong, M. J., Wang, S. H., Reid, J. S., Liou, K. N., and Ou, S. C.: An Assessment of the Surface Longwave Direct Radiative Effect of Airborne Saharan

- Dust during the NAMMA Field Campaign, *J. Atmos. Sci.*, 67, 1048–1065, <https://doi.org/10.1175/2009JAS3257.1>, 2010.
- He, L., Wang, L., Li, Z., Jiang, D., Sun, L., Liu, D., Liu, L., Yao, R., Zhou, Z., and Wei, J.: VIIRS Environmental Data Record and Deep Blue aerosol products: validation, comparison, and spatiotemporal variations from 2013 to 2018 in China, *Atmos. Environ.*, 250, 118265, <https://doi.org/10.1016/j.atmosenv.2021.118265>, 2021.
- Huang, Z., Huang, J., Bi, J., Wang, G., Wang, W., Fu, Q., Li, Z., Tsay, S.-C., and Shi, J.: Dust aerosol vertical structure measurements using three MPL lidars during 2008 China-U.S. joint dust field experiment, *J. Geophys. Res.-Atmos.*, 115, D00K15, <https://doi.org/10.1029/2009JD013273>, 2010.
- Huang, Z., Huang, J., Hayasaka, T., Wang, S., Zhou, T., and Jin, H.: Short-cut transport path for Asian dust directly to the Arctic: a case study, *Environ. Res. Lett.*, 10, 114018, <https://doi.org/10.1088/1748-9326/10/11/114018>, 2015.
- Huang, Z., Nee, J.-B., Chiang, C.-W., Zhang, S., Jin, H., Wang, W., and Zhou, T.: Real-Time Observations of Dust-Cloud Interactions Based on Polarization and Raman Lidar Measurements, *Remote Sens.*, 10, 1017, <https://doi.org/10.3390/rs10071017>, 2018.
- Huang, Z., Qi, S., Zhou, T., Dong, Q., Ma, X., Zhang, S., Bi, J., and Shi, J.: Investigation of aerosol absorption with dual-polarization lidar observations, *Opt. Express*, 28, 7028, <https://doi.org/10.1364/OE.390475>, 2020.
- Huang, Z., Wang, Y., Bi, J., Wang, T., Li, W., Li, Z., and Zhou, T.: An overview of aerosol lidar: progress and prospect, *National Remote Sensing Bulletin*, 26, 834–851, <https://doi.org/10.11834/jrs.20221388>, 2022.
- Huang, Z., Dong, Q., Chen, B., Wang, T., Bi, J., Zhou, T., Alam, K., Shi, J., and Zhang, S.: Method for retrieving range-resolved aerosol microphysical properties from polarization lidar measurements, *Opt. Express*, 31, 7599, <https://doi.org/10.1364/OE.481252>, 2023a.
- Huang, Z., Li, M., Bi, J., Shen, X., Zhang, S., and Liu, Q.: Small lidar ratio of dust aerosol observed by Raman-polarization lidar near desert sources, *Opt. Express*, 31, 16909, <https://doi.org/10.1364/OE.484501>, 2023b.
- IPCC: Climate Change 2013: The Physical Science Basis. Contribution of Working Group I to the Fifth Assessment Report of the Intergovernmental Panel on Climate Change, edited by: Stocker, T. F., Qin, D., Plattner, G.-K., Tignor, M., Allen, S. K., Boschung, J., Nauels, A., Xia, Y., Bex, V., and Midgley, P. M., Cambridge University Press, Cambridge, United Kingdom and New York, NY, USA, 1535 pp., 2013.
- Ke, J., Sun, Y., Dong, C., Zhang, X., Wang, Z., Lyu, L., Zhu, W., Ansmann, A., Su, L., Bu, L., Xiao, D., Wang, S., Chen, S., Liu, J., Chen, W., and Liu, D.: Development of China's first space-borne aerosol-cloud high-spectral-resolution lidar: retrieval algorithm and airborne demonstration, *PhotonIX*, 3, 17, <https://doi.org/10.1186/s43074-022-00063-3>, 2022.
- Lakshmi, N. B., Nair, V. S., and Babu, S. S.: Assessment of the vertical distribution of speciated aerosol absorption over South Asia using spaceborne LIDAR and ground-based observations, *Remote Sens. Environ.*, 253, 112164, <https://doi.org/10.1016/j.rse.2020.112164>, 2021.
- Liu, D., Zheng, Z., Chen, W., Wang, Z., Li, W., Ke, J., Zhang, Y., Chen, S., Cheng, C., and Wang, S.: Performance estimation of space-borne high-spectral-resolution lidar for cloud and aerosol optical properties at 532 nm, *Opt. Express*, 27, A481, <https://doi.org/10.1364/OE.27.00A481>, 2019.
- Liu, Q., Huang, Z., Hu, Z., Dong, Q., and Li, S.: Long-Range Transport and Evolution of Saharan Dust Over East Asia From 2007 to 2020, *J. Geophys. Res.-Atmos.*, 127, e2022JD036974, <https://doi.org/10.1029/2022JD036974>, 2022.
- Mamouri, R. E., Amiridis, V., Papayannis, A., Giannakaki, E., Tsaknakis, G., and Balis, D. S.: Validation of CALIPSO spaceborne-derived attenuated backscatter coefficient profiles using a ground-based lidar in Athens, Greece, *Atmos. Meas. Tech.*, 2, 513–522, <https://doi.org/10.5194/amt-2-513-2009>, 2009.
- Marcos, C. R., Pedrós, R., Gómez-Amo, J. L., Utrillas, M. P., and Martínez-Lozano, J. A.: Analysis of Desert Dust Outbreaks Over Southern Europe Using CALIOP Data and Ground-Based Measurements, *IEEE T. Geosci. Remote*, 54, 744–756, <https://doi.org/10.1109/TGRS.2015.2464701>, 2016.
- NASA: CALIPSO Search and Subsetting web application, NASA [data set], <https://subset.larc.nasa.gov/calipso/> (last access: 9 November 2023), 2023.
- Qi, S., Huang, Z., Ma, X., Huang, J., Zhou, T., Zhang, S., Dong, Q., Bi, J., and Shi, J.: Classification of atmospheric aerosols and clouds by use of dual-polarization lidar measurements, *Opt. Express*, 29, 23461, <https://doi.org/10.1364/OE.430456>, 2021.
- Sugimoto, N. and Huang, Z.: Lidar methods for observing mineral dust, *J. Meteorol. Res.*, 28, 173–184, <https://doi.org/10.1007/s13351-014-3068-9>, 2014.
- Sugimoto, N., Huang, Z., Nishizawa, T., Matsui, I., and Tatarov, B.: Fluorescence from atmospheric aerosols observed with a multi-channel lidar spectrometer, *Opt. Express*, 20, 20800, <https://doi.org/10.1364/OE.20.020800>, 2012.
- Tao, Z., McCormick, M. P., and Wu, D.: A comparison method for spaceborne and ground-based lidar and its application to the CALIPSO lidar, *Appl. Phys. B*, 91, 639–644, <https://doi.org/10.1007/s00340-008-3043-1>, 2008.
- Vaughan, M. A., Young, S. A., Winker, D. M., Powell, K. A., Omar, A. H., Liu, Z., Hu, Y., and Hostetler, C. A.: Fully automated analysis of space-based lidar data: an overview of the CALIPSO retrieval algorithms and data products, *Remote Sensing, Maspalomas, Canary Islands, Spain*, 13–16 September 2004, 16, *Laser Radar Techniques for Atmospheric Sensing*, <https://doi.org/10.1117/12.572024>, 2004.
- Wang, Q., Mustafa, F., Bu, L., Yang, J., Fan, C., Liu, J., and Chen, W.: Monitoring of Atmospheric Carbon Dioxide over a Desert Site Using Airborne and Ground Measurements, *Remote Sens.*, 14, 5224, <https://doi.org/10.3390/rs14205224>, 2022.
- Wang, S., Ke, J., Chen, S., Zheng, Z., Cheng, C., Tong, B., Liu, J., Liu, D., and Chen, W.: Performance Evaluation of Spaceborne Integrated Path Differential Absorption Lidar for Carbon Dioxide Detection at 1572 nm, *Remote Sens.*, 12, 2570, <https://doi.org/10.3390/rs12162570>, 2020.
- Wang, W., Gong, W., Mao, F., and Pan, Z.: Physical constraint method to determine optimal overlap factor of Raman lidar, *J. Opt.*, 47, 83–90, <https://doi.org/10.1007/s12596-017-0427-9>, 2018.
- Winker, D. M., Vaughan, M. A., Omar, A., Hu, Y., Powell, K. A., Liu, Z., Hunt, W. H., and Young, S. A.: Overview of the CALIPSO Mission and CALIOP Data Processing Algorithms, *J. Atmos. Ocean. Tech.*, 26, 2310–2323, <https://doi.org/10.1175/2009jtecha1281.1>, 2009.

- Zha, C., Bu, L., Li, Z., Wang, Q., Mubarak, A., Liyanage, P., Liu, J., and Chen, W.: Aerosol Optical Properties Measurement using the Orbiting High Spectral Resolution Lidar onboard DQ-1 Satellite: Retrieval and Validation, *Atmos. Meas. Tech. Discuss.* [preprint], <https://doi.org/10.5194/amt-2023-219>, in review, 2023.
- Zhang, S., Huang, Z., Li, M., Shen, X., Wang, Y., Dong, Q., Bi, J., Zhang, J., Li, W., Li, Z., and Song, X.: Vertical Structure of Dust Aerosols Observed by a Ground-Based Raman Lidar with Polarization Capabilities in the Center of the Taklimakan Desert, *Remote Sens.*, 14, 2461, <https://doi.org/10.3390/rs14102461>, 2022.
- Zhang, S., Huang, Z., Alam, K., Li, M., Dong, Q., Wang, Y., Shen, X., Bi, J., Zhang, J., Li, W., Li, Z., Wang, W., Cui, Z., and Song, X.: Derived Profiles of CCN and INP Number Concentrations in the Taklimakan Desert via Combined Polarization Lidar, Sun-Photometer, and Radiosonde Observations, *Remote Sens.*, 15, 1216, <https://doi.org/10.3390/rs15051216>, 2023.